Composite Structures 334 (2024) 117972

Contents lists available at ScienceDirect

Composite Structures

journal homepage: www.elsevier.com/locate/compstruct

Damage monitoring of pinned hybrid composite–titanium joints using direct current electrical resistance measurement

Andreas Dengg *, Christoph Kralovec, Martin Schagerl

Institute of Structural Lightweight Design, Johannes Kepler University, Altenberger Straße 69, Linz, 4040, Upper Austria, Austria

ARTICLE INFO

Keywords:
Structural health monitoring
Pin-reinforced joint
Hybrid joint
Composite–metal joint
Electrical resistance measurement
Structural analysis

ABSTRACT

The present research addresses structural health monitoring of pinned, composite–titanium (i.e.: hybrid) joints with the aim of using their lightweight potential and damage tolerance in future aircraft designs. Together with additively manufactured titanium pins, protruding into the carbon-fiber composite, a single-lap shear joint specimen is monitored with direct current electrical resistance measurements (DC ERM) across the overlap, without conductivity-enhancing additives (e.g., carbon nanotubes), but rather with the pins' complex electrical network that forms with the carbon-fiber composite. For a proof-of-concept demonstration, a structural test with quasi-static, tension–tension loading and unloading is performed. Using digital image correlation, degradation of the joint is monitored. Results are validated by a 2-dimensional finite element model, considering multiple damage states. For DC ERM, a damage indicator is proposed to evaluate the joint's structural condition. It is shown that typical damage for this joint type reported literature (i.e., cracks occurring at the overlap ends) could be reproduced and detected by the electrical property change across the overlap. Under the given laboratory conditions, the proposed DC ERM damage indicator clearly shows a non-reversible increase in resistance by 3.8% due to damage, starting at first damage initiation and also reflecting further damage growth. Thereby, the method's capability for damage detection and monitoring is demonstrated.

1. Introduction

For the construction of large civil aircraft structures, mechanical fasteners like rivets and bolts are commonly used despite their added weight to the design. In contrast to those mechanical joints, there is still not much confidence in adhesive bonding of aircraft components, since its structural properties vary strongly with manufacturing process quality. This is particularly true for the joining of different materials (i.e., hybrid joints). With the goal of reducing the ecological impact of aircraft production and operation, circular economy with the exploitation of various different materials must be considered as early as possible in the design of future aircraft. So-called pinned hybrid metal–composite joints realize a structural connection with the help of metallic pins on the surface of the metal adherend, protruding into the composite joining partner, thus interlocking with the fiber–matrix combination. For composite materials with a thermoset matrix, the metal pins are introduced before the matrix curing process. That way, an adhesive bond as well as a mechanical connection are created, without additional adhesive for creating the joint. This type of co-bonded joint may have less strength because the composite's matrix material generally does not have the properties of application-specific structural adhesives. However, the use of such joints has advantages such as very thin adhesive layers (here the matrix of the composite) and simpler design [1]. Furthermore, the number of manufacturing steps can be reduced since additional adhesive application is not required. Nevertheless, static and cyclic structural investigations show that pinned composite–metal joints possess higher damage tolerance than comparable bonded joints without pins. Among the first, Ucsnik et al. carried out experimental work on pinned, hybrid double-lap shear (DLS) specimens with cold-metal transfer steel pins and a carbon fiber-reinforced polymer (CFRP) [2]. Static and cyclic fatigue tests on pinned hybrid single-lap shear (SLS) specimens were carried out by Parkes et al. with additively manufactured pins, investigating the joint's damage modes with c-scans, and the joint's damage tolerance. In the static investigations, the pinned joint's ultimate tensile strength was 6.5 times larger than the values of unpinned reference joints. [3,4]. Comprehensive structural experiments are reported by Graham et al. for DLS and SLS joints with various manufacturing approaches and material combinations. Specimens without pinned joints served as reference and its strength values were significantly lower than those of the pinned specimens [5]. Huelsbusch et al. investigated pin size

* Corresponding author.
E-mail address: andreas.dengg@jku.at (A. Dengg).

https://doi.org/10.1016/j.compstruct.2024.117972
Received 3 July 2023; Received in revised form 27 November 2023; Accepted 9 February 2024
Available online 10 February 2024

influence of additive manufactured pins for composite–titanium SLS specimens under quasi-static and cyclic loading and assessed occurring damage mechanisms. [6]. Sarantinos et al. give an overview of through-the-thickness reinforced composites in joints with a selection of case examples of composite to metal joints and different manufacturing methods of pins, comparing the improved properties to conventional adhesively bonded joint variants [7]. Determining design parameters for desired joint properties and the identification and prediction of their associated failure modes for different loading types are active fields of research. When considering a SLS geometry with one overlap (i.e., the location of the joint where the two adherends overlap), introduced pins influence the strain and stress distribution along said overlap. Nevertheless, there are many similarities to the theory of adhesively bonded joints, especially at the overlap ends, where pins are often not in the proximity and the composite matrix acts as adhesive material to the metal adherend. For these adhesively bonded and tensile loaded SLS joints, established theories [8,9] provide the highest values of shear stress at these overlap ends. Consequently, also for the presently considered pinned hybrid SLS joints, these locations are extremely susceptible to damage initiation and following damage propagation until failure [5,10,11]. A possible approach to guarantee the integrity of a pinned hybrid SLS joint is structural health monitoring (SHM). SHM can be realized on different levels of implementation, with the first level being damage detection in general [12,13]. The other levels are: Damage location (level 2), damage quantification (level 3) and damage typification (level 4). In general, a variety of SHM methods and corresponding sensor systems are available, all of which are sensible to specific, inherent physical properties of the monitored structure. Thus, when the initial and critical (i.e., safety relevant) damage types and their influence on the physical properties of the host structure are known, particular, most sensitive SHM methods can be selected and tailored for the monitoring task. Electrical resistance measurement (ERM) as SHM method uses the non-reversible resistance change of a bulk material or an interface, if damage occurs.

As far as the bulk material is concerned, among others, Abry et al. investigated resistance changes of CFRP material and their origin in the changing physical conducting paths inside [14], later on demonstrating in-situ damage detection with ERM [15]. Zhao et al. give an extensive overview over usable effects that change the electrical behavior of CFRP material, which is also related to the mechanical integrity [16]. Angelidis et al. investigated the electrical current distribution inside continuous carbon fiber composites under mechanical loading, among other things, with the help of gauge factor determination for different laminates and directions [17]. As far as joint interfaces are concerned, Chung et al. conducted DC ERM measurements on CFRP interfaces for findings about contact resistance change during loading [18]. Till et al. investigated health monitoring with ERM of a scarfed composite–composite joint, using adhesive films that are electrically modified with carbon nanotubes and further adding dedicated conductive paths [19]. Further, Lim et al. investigated both direct current ERM and Acoustic Emission (AE) for increasing cyclic loading and unloading of an adhesively bonded composite-stainless steel SLS specimen [20]. Depending on the electrical properties of the monitored structure, alternating current (AC) or direct current (DC) ERM are favorable for SHM. For monitoring CFRP, the selection between AC and DC methods is typically governed by the question, whether the considered damage mode is a fiber-dominated or a matrix-dominated one. Especially for matrix-dominated failure, the AC methods are favored, as the use of DC ERM as early damage detection in bulk CFRP material is challenging [21]. However, DC ERM is less elaborate in practice than AC ERM and therefore, also used for damage monitoring for interfaces of adhesive joints, where matrix-dominant failure occurs [22]. This is made possible by adding carbon nanotubes to the adhesive to enhance its electrical conductivity. Damage monitoring typically applies the non-reversible resistance change due to damage-induced material separation for evaluation. Additionally, CFRP bulk material shows a piezoresistive effect, i.e., its electrical resistance is strain-dependent. Apart from the sole bulk material, both resistance-changing effects are also observed at interfaces of CFRP with other electrically conductive materials, e.g., metals. The conductive carbon fibers, embedded in an isolating matrix, form a complex electrical network. With the metal surface in contact with and the pins protruding into the composite, a conductive interface across the hybrid joint is formed, resulting in interfacial, piezoresistive properties.

In the present research, the focus is primarily on the proof-of-concept of the SHM method of DC ERM with its novel damage evaluation presented here. A pinned hybrid composite-titanium joint (without costly electrical modifications) serves as a novel case example for the reasons given above. With the occurrence of damage in the form of cracks at the overlap ends and subsequent damage propagation, the inherent electrical network is changed and electrical properties of the interface respond accordingly. Thus, for DC ERM method application, the global piezoresistive effect of the adherends and the pinned interface must be taken into account. For the purpose of damage monitoring with DC ERM, structural and electrical investigations are performed. They are reported as follows: In Section 2, the used specimen and its preparation are described. The experimental setup is shown and the applied methods are presented. These are the digital image correlation (DIC) for surface crack identification and overlap stiffness evaluation and a finite element (FE) model used to analyze and validate the measured results. The DC ERM method for non-reversible resistance change identification is introduced together with a damage indicator proposed for damage evaluation. In Section 3, all experimental and numeric results are presented and discussed to reliably monitor the specimen's structural degradation, and subsequently, demonstrate the correlation of the degradation with the non-reversible electrical resistance change. Final conclusions of the research are given in Section 4.

2. Materials and methods

In the present study, the presented SHM method of DC ERM is demonstrated. For detailed structural investigations of the joint, it would be necessary for statistical significance to test at least three specimens identically. The positive effect of the pins on the considered hybrid SLS joint design was found by a cooperating research group and will be published soon. However, for this proof-of-concept SHM demonstration, only one specimen is available to the authors, which gets described in Section 2.1. In terms of DC ERM, this circumstance is addressed and compensated by multiple, recurring loading and unloading cycles for more available data, which get presented together with the experimental setup in Section 2.2. Following this consistent approach, detailed evaluation of the joint degradation behavior is performed with the help of DIC methods described in Sections 2.3 and 2.4, as well as with the help of a numerical investigation described in Section 2.5. The proposed DC ERM method is presented in Section 2.6.

2.1. Test specimen geometry and preparation

In Fig. 1, the prepared test specimen is shown schematically together with information about the used pin geometry and the pin array. The overall geometry of the SLS specimen is based on ASTM D5868 [23]. The two different adherend materials are: One titanium sheet metal strip made of generic, industrial grade Ti-6Al-4V with additively manufactured pins (Laser Powder Bed Fusion [24], performed at the DLR Institute of Materials Research in Köln, Germany), arranged in a defined array and one epoxy resin based CFRP adherend, consisting of a symmetrical layup with six plies $[0/45/0]_s$, made of 5-harness (5H) satin weave fabric and the warp direction defined as 0°. The used fabric is a HexForce© G0926 D 1304 TCT HS06K [25] and the used epoxy matrix is a HexPly© 913 [26], both provided by HEXCEL© Corp. (Stamford, Connecticut, United States of America). Samples are manufactured inside a professional, industry-standard

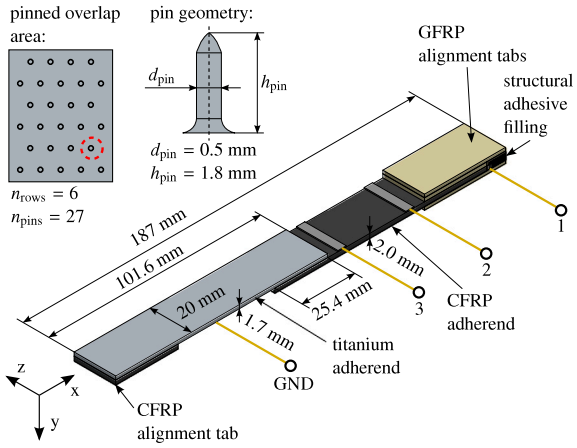

Fig. 1. Schematic presentation of the pinned hybrid SLS specimen and four applied electrical contacts.

composite production environment at INVENT GmbH (Braunschweig, Germany), starting with five titanium adherends held inside a purpose-built tool. Hand layup is performed with the pre-impregnated fabric layers being pushed against all five dust- and grease-free pinned overlap areas until the pins are incorporated into the layup. Subsequently, the setup is vacuum-bagged and cured in an autoclave process. By complying with the autoclave curing process specified by the CFRP manufacturer, a nominal resin volume content of 35% can be assumed, as given in the data sheet. This resin volume content may vary locally, possibly also in the region of the overlap. However, this variation is kept low by the combined production of five specimens per CFRP layup and used border plates, which reduce the outflow of resin during autoclave curing. Afterwards, the CFRP is cut with a diamond saw blade to the dimensions shown. Alignment tabs made of glass fiber reinforced polymer (GFRP) and CFRP are bonded to the ends. This ensures aligned clamping conditions relative to the overlap during structural testing. Four electrical contacts are applied to the specimen: For the titanium adherend, an electrical wire is bonded to the clean, bare metal surface with the help of electrically conducting silver epoxy EPO-TEK© H20E supplied by Epoxy Technology Inc. (Billerica, Massachusetts, United States of America). For the CFRP adherend, the surface is laser engraved on two locations to contact the carbon fibers, a contacting method that is readily reported in literature [27,28]. In the present work, matrix material of the areal size of 4 × 20 mm^2 is removed from the composite surface to expose the outermost fibers for every electrical contact. After cleaning with isopropyl alcohol, the fibers get contacted to electrical wires with the same silver epoxy material as is used for the titanium adherend. The remaining contact is established at the rear end of the CFRP adherend with the help of chemically etching the composite layers with 95% sulfuric acid to expose the fiber ends [29]. After rinsing the etched area with purified water and air drying, a silver-epoxy bond is created across all woven composite layers to an electrical wire. Two additional glass fiber tabs are added with Scotch-Weld™ Epoxy Adhesive DP490, supplied by 3M (Saint Paul, Minnesota, United States of America), to the specimen for electrical isolation of the contact during clamping inside the test rig. The resulting cavity at the rear end is filled with the same epoxy adhesive for mechanical protection. Finally, the specimen is coated with white spray paint for better observation of cracks and as primer for a high contrast, random speckle pattern, which is applied for DIC measurements at the lateral surface of the joint.

2.2. Experimental setup and procedure

The experimental setup is shown in Fig. 2. During the experiment, the specimen is clamped by hydraulic grips at both ends and is loaded

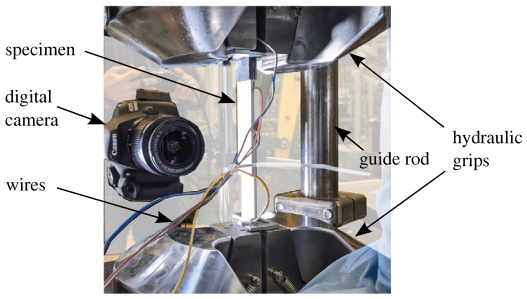

Fig. 2. Experimental setup with the spray painted and speckled specimen, clamped between two guided hydraulic grips, four wires electrically contacted to the specimen and the digital camera.

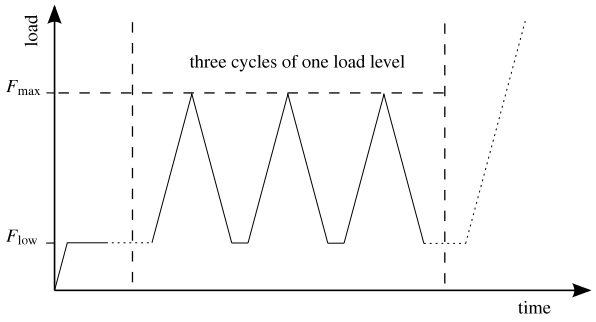

Fig. 3. Cycle and load level definition.

along its longitudinal axis. To prevent load misalignment and to ensure only axial loading by the test rig, both hydraulic grips are initially aligned and guided by sliding bearings along 3 guide rods. With the goal of collecting sufficient data for DC ERM method application, a servo-hydraulic cylinder exposes the specimen to multiple cycles of quasi-static, tension–tension loading and unloading force F with a crosshead speed of 0.2 mm/min. The cycles are described in Fig. 3. The lower tension load has a value of F_{low} = 320 N. The first higher tension load applied is F_{max} = 1.2 kN. After three cycles, F_{max} is increased by 1 kN to 2.2 kN. For some cycles, a smaller increment than 1 kN is used to collect more data. The procedure continues until final rupture of the specimen. The presented work focuses on the loading part of the cycles, because damage growth (i.e., crack propagation) is expected to be dominant in this part. Crosshead displacement and applied load are recorded continuously with a sampling rate of 300 Hz. All data is stored in a time synchronous manner. The optical method of 2-dimensional DIC is used in this experiment for obtaining crack lengths and structural stiffness evaluation of the joint. A single digital camera and adequate lighting conditions are set up. During all cycles, digital pictures are taken automatically every second from the speckled surface. The idealized electrical network assumed for the electrical measurements at the considered specimen is presented in Fig. 4 (see Fig. 1 for true locations of the electrical contacts). The GND is located at the titanium adherend. The electric contact 1 (at the CFRP adherend end) is used to introduce a constant current of I = 10 mA with a Keithley 6220 precision current source. The CFRP surface contacts 2 and 3 are used to measure the electric potential to GND with a HBM QuantumX MX840A data acquisition system. Electrical measurements are recorded continuously per cycle. Between the single cycles at F_{low}, they are interrupted for other measurements that are not part of the present study. The sampling rate of the measured electrical potentials for DC ERM is 300 Hz.

2.3. Damage evaluation by surface crack observation

Experiments at the authors' laboratory and literature show that the cracks at the overlap ends quickly extend across the entire width of the

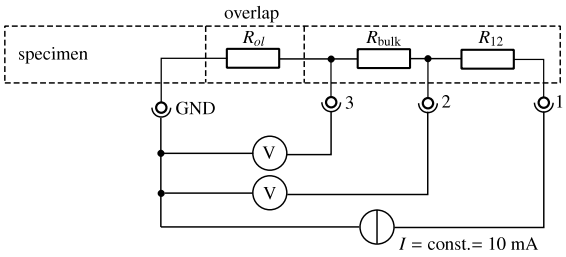

Fig. 4. Schematic view of the DC ERM setup and the idealized electrical network.

joint [3,5,11]. Thus, it is sufficient to experimentally observe the lateral surface of the joint to capture the extent of the damage. Traditionally, surface crack propagation is observed by optical microscopy [30]. However, in the present study, a DIC system is used as the accuracy is sufficient for the demonstration of the proposed SHM method and the strain field is recorded. A twofold crack observation with DIC camera and optical microscope was not possible due to geometric constraints at the test rig (cf., Fig. 2). The DIC software used to analyze the recorded digital images is Vic-2D 6, provided by Correlated Solutions Inc. Camera and DIC parameters are presented in Table 1. The evaluation of the two crack lengths at the overlap ends uses the spatial one-standard deviation confidence (Vic-2D output variable sigma in pixel) of the continuously recorded DIC images, which get compared to an initial reference image [31,32]. The spatial one-standard deviation confidence is estimated based on the gray value standard deviation of pixel subsets, thus, a low standard deviation indicates a high confidence in the spatial correlation of the subsets (i.e., accuracy of the measurement results) and vice versa [33]. In the present paper, the spatial one-standard deviation confidence is referred as "correlation confidence". The correlation confidence cannot be calculated directly from the DIC images, but is approximated in Vic-2D from the DIC image gray value standard deviation per pixel subset. Consequently, the correlation confidence for the recorded speckle pattern is influenced by anything that changes the image's gray values, like e.g., specimen displacement, lighting condition changes and speckle pattern damage [33]. For typical DIC imaging conditions (little displacement and strain and no change in lighting), the latter has a large effect on the gray scale values, and thus, the correlation confidence can be used for surface crack observation at an investigated specimen (assuming bonding between the speckle pattern and the specimen surface). This method has already proven to be useful in crack evaluation and other composite damage types [34–36]. In the present research, a correlation confidence threshold value is determined, which indicates whether a crack is present or not. This threshold value is defined based on the two ultimate crack lengths determined at the ruptured specimen (visual post-test analysis of the ruptured joint surfaces) and the correlation confidence values of the last recorded image before specimen rupture. The area where the correlation confidence exceeds the defined threshold value is considered cracked, and thus, enables to observe its length and growth. This approach for crack length evaluation in adhesively bonded SLS joints was demonstrated by [37] with strain value thresholds. It must be noted that due to the correlation procedure, DIC results do not reach up to the free edge of the specimen. Therefore, with the selected DIC subset and step size, determining crack lengths below approximately 0.8 mm to the specimen's free edge is not possible.

2.4. Damage evaluation by tangent stiffness degradation

The stiffness of a joint includes all kind of degradation effects. Thus, effects that are not reflected by the formation and propagation of a surface crack also become visible. For SLS specimens, literature reports a nonlinear stiffness behavior with respect to an uniaxial tension load F [5]. Furthermore, nonlinear stiffness behavior results from

Table 1
Camera and 2D-DIC parameters.

Parameter	Value
Camera resolution	18 MP
Focal length	55 mm
Camera distance	120 mm
Subset size	63 px (0.84 mm)
Step size	16 px (0.12 mm)

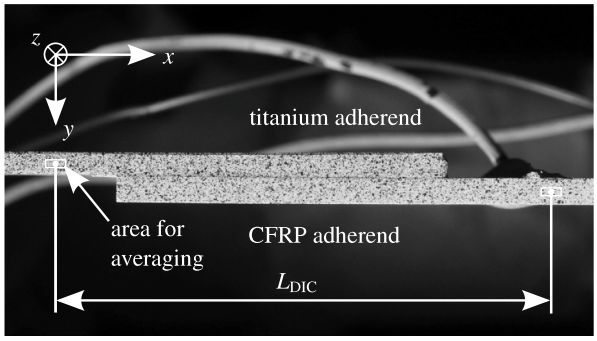

Fig. 5. Length L_{DIC} spanning over the SLS joint for calculation of tangent stiffness k_{tan}. Areas for averaging are shown for the two distance points.

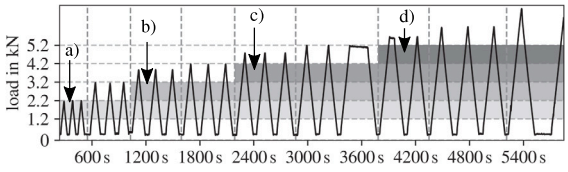

Fig. 6. Load ranges in kN used for evaluation, highlighted in the experiment's recorded load signal: (a) [1.2, 2.2], (b) [2.2, 3.2], (c) [3.2, 4.2] and (d) [4.2, 5.2].

potentially occurring damage D. That is why tangent stiffness $k_{tan}(D)$ is used to evaluate the joint's degradation. Tangent stiffness is defined as:

$$k_{tan}(D) = \frac{\partial F}{\partial L} \tag{1}$$

In the present work, L describes a distance which spans across the joint. During the experiment, the change of distance is obtained with DIC from two selected points, i.e., $L = L_{DIC}$. The used distance is shown in Fig. 5. At the two end points of the distance, the areas for averaging DIC displacement are shown, which leads to less noise in the final values. Subsequently, $k_{tan}(D)$ gets calculated numerically. For validation of the obtained values by a FE model (see Section 2.5), the procedure for the calculation of $k_{tan}(D)$ is conducted with the same points, i.e., $L = L_{FE}$. The calculated $k_{tan}(D)$ is averaged over defined load ranges to reduce scattering. The load ranges in kN are [1.2, 2.2], [2.2, 3.2], [3.2, 4.2] and [4.2, 5.2]. For better understanding, Fig. 6 shows the complete load over time plot of the considered experiment with the evaluated load ranges indicated by gray shaded bars.

2.5. Numerical investigation

The numerical investigation uses a 2D FE model with the goal of qualitatively analyzing the influence of overlap end damage and its propagation through the overlap on the joint's tangent stiffness. For this purpose, displacement results of the 2D FE model are of interest. The method allows a model-based validation of the experimental stiffness results. Abaqus 2019 software [38] is applied for modeling and simulation. The components of the 2D FE model (i.e., geometry, mesh, materials, element properties, boundary conditions, constraints and

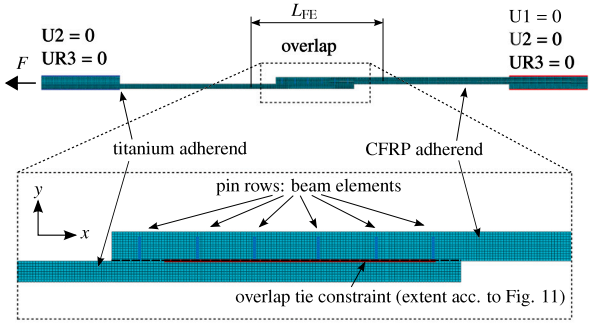

Fig. 7. 2D FE model for numerical calculation of damage-dependent tangent stiffness.

applied loads) are modeled with assumptions derived from the real conditions in the conducted experiment. The geometry of the specimen is represented by a 2D section, that is meshed with 4-node bilinear plane strain elements (formulation CPE4 in Abaqus). There are 12 elements across the 2.0 mm thick composite adherend and eight elements across the 1.7 mm thick titanium adherend. Single pins cannot be modeled in a 2D FE model. For a qualitative representation of the stiffness increasing effect of the six pin rows, six beams with a rectangular cross section are introduced along the overlap. The joint stiffness contribution of the pins is considered to be dominated by its bending stiffness. Thus, the six modeled beam sections were defined such that their bending stiffnesses are equivalent to their respective pin row (can be four or five pins per row, cf. Fig. 1). One beam is meshed with ten 3-node quadratic 2D elements (formulation B22 in Abaqus) along its height. A convergence study shows independence of the deformation results from the defined discretization. An overview of the model is given in Fig. 7. Geometrical coupling of the pin roots to the titanium adherend's mesh and tie constraints of all beam nodes to the composite adherend's mesh take the added stiffness of the pins into account. The mesh is created so that all constrained nodes are congruent, thus, keeping coupling distances at a minimum. Furthermore, the coupling between the two adherends is realized with a tie constraint, thus, assuming perfect bonding. Different states of overlap damage are modeled by opening this tie constraint at crack locations (i.e., where the DIC-based observation of the tested specimen indicates a crack). For comparison, nine pristine and damage states are considered, that are approximated and uniformly distributed with respect to the experimentally identified ultimate crack length. For optimal comparison between simulated and experimental results, overlap crack lengths are used that fit the FE model's discretization. For modeling a damaged pin row, the geometric coupling at the pin row's root is deactivated. This is performed later for the two outermost pin rows, situated on the far left and far right of the overlap, shown in Fig. 7. For the titanium adherend, isotropic material behavior is considered. Used values of the datasheet [39] are listed in Table 2. For the CFRP adherend, orthotropic material behavior is considered. Equivalent laminate properties of the given layup are derived according to [40] with the main ply properties taken from the datasheet [26]. Equivalent material properties used for the FE model are listed in Table 2, with the material orientation coordinate system (123) aligned with the global coordinate system (xyz).

Boundary conditions are defined along the nodes representing the clamping situation imposed by the test rig: Translatory degrees of freedom (DOF) U1, U2 as well as rotational DOF UR3 are locked for the titanium adherend, which is clamped at the hydraulic grip at the bottom (cf., Fig. 2). DOF U2 and UR3 are locked for the CFRP adherend, which is clamped at the axially guided hydraulic grip at the top. For tensile loading, 10 kN are applied in x-direction to the end of the CFRP adherend. Geometrically nonlinear analysis with the Abaqus/Standard solver is conducted in 50 linearly distributed steps. For comparison with experimental tangent stiffness evaluation, displacement values of

Table 2
Material properties used for the FE model.

Property	Unit	CFRP layup $[0/45/0]_s$	Titanium
E_1	GPa	61.0	
E_2	GPa	21.8	110.0
E_3	GPa	62.0	
G_{31}	GPa	12.6	
G_{23}	GPa	10.4	
G_{12}	GPa	10.4	
ν_{31}	–	0.14	
ν_{21}	–	0.1	0.31
ν_{23}	–	0.1	

two areas left and right of the overlap (exactly the same locations as used in the experimental evaluation) are used to obtain the change of the distance L_{FE} (cf. Fig. 7).

2.6. Electrical resistance as damage indicator

As shown in Fig. 4, the specimen is idealized by three electrical resistances. Only the resistances representing the bulk CFRP material (i.e., R_{bulk}, between contacts 2 and 3) and the overlap (i.e., R_{ol}, between contacts 3 and GND) are of interest for the present investigation. For the proposed DC ERM method, the electrical resistance of the overlap R_{ol} is assumed to be sensitive to damage D (i.e., cracks at the overlap ends). However, due to the specific electrical properties of the overlap, the resistance R_{ol} is also dependent on temperature and mechanical strain ε. In the present study, temperature influence can be neglected due to laboratory conditions and a linear strain dependence is assumed.

To model the overlap resistance R_{ol}, the piezoresistive behavior of the overlap's interface and the non-reversible increase in resistance due to damage need to be considered. Therefore, the overlap resistance is separated into two theoretical resistances in serial connection, with the purpose of separating the purely strain-dependent pristine (superscript p) and damaged (superscript d) behavior:

$$R_{ol}(\varepsilon, D) = R^{p}(\varepsilon) + R^{d}(\varepsilon, D). \tag{2}$$

A Taylor expansion along variable ε is performed, which yields the following expression. All higher terms are already neglected:

$$R_{ol}(\varepsilon, D) \approx R_0^{p} + R_0^{p}GF^{p}\varepsilon + R^{d}(0, D) + O^{d}(\varepsilon, D). \tag{3}$$

The specimen's pristine resistance under no strain is R_0^{p} and its linear strain behavior is described by the gauge factor GF^{p}, as known from literature [17,18,41]. $R^{d}(0, D)$ represents the non-reversible resistance change due to damage D under no strain. This strain- and therefore load-independent value, is proposed as damage indicator (DI) for overlap damage evaluation. The second damage-related term $O^{d}(\varepsilon, D)$ relates to a strain-dependent behavior of the non-reversible resistance change. According to Fig. 18(c), its influence is low and thus, plays a minor role. Aware of this fact, the evaluations are nevertheless carried out at low load values (load range [1.2, 2.2] kN, cf. Fig. 6a) to minimize the term's potential influence. After rearrangement of Eq. (3) and neglection of $O^{d}(\varepsilon, D)$, the proposed $DI = R^{d}(0, D)$ is written as:

$$DI = R_{ol}(\varepsilon, D) - R_0^{p}(1 + GF^{p}\varepsilon) \tag{4}$$

In this work, the gauge factor GF^{p} and R_0^{p} are found by linear regression. The same procedure for gauge factor determination is performed on the bulk CFRP material's resistance R_{bulk} for the purpose of comparison. In the bulk material, it is assumed that no resistance changing damage occurs. The assumption of linear strain dependence is checked by calculating the coefficient of determination (COD) for the linear regression of the measured resistances.

Table 3
Loading cycles performed during test.

Cycle no.	Load level F_{max} in kN
(1, 2, 3)[a]	1.2
4, 5, 6	2.2
7, 8, 9	3.2
10, 11, 12	3.9
13, 14, 15	4.2
16, 17, 18	4.8
19, 20, 21	5.2
22, 23[b]	5.7
24, 25, 26	6.2
27, 28[c]	7.2

[a] Not used due to test rig friction issues.
[b] Unscheduled test program pause led to two cycles.
[c] Specimen ruptured at $F_{ultimate}$ = 6.65 kN, during the second cycle.

3. Results and discussion

In this section, first, a short overview of the response of the considered pinned hybrid SLS specimen to the mechanical loading including a post-test fracture analysis is given. Second, the crack initiation and crack propagation at the overlap during testing is evaluated and presented, based on DIC measurements. Third, the overall structural degradation during testing, represented by the joint's tangent stiffness $k_{tan}(D)$ is also evaluated and presented, based on DIC measurements. Fourth, the experimentally determined crack propagation and joint stiffness degradation are validated by FE model-based simulations. Fifth, the results of the DC ERM method are presented and the determination of the proposed DI value is explained in detail. And finally, the DI sensitivity to the considered overlap damage is demonstrated by correlation to the measured joint degradation and crack lengths.

3.1. Mechanical loading and post-test analysis

The quasi-static, cyclic tensile–tensile loading was done according to Fig. 3. The performed load levels are summarized in Table 3. For F_{max} = 5.7 kN, two instead of three cycles are available due to an unscheduled test program pause. The specimen failed at $F_{ultimate}$ = 6.65 kN, during the second cycle with F_{max} = 7.2 kN. Results of the experiment reflect the typical type of damage initiation and propagation reported in literature for such pinned hybrid joints (i.e., cracks at the overlap ends and their propagation towards the overlap's longitudinal center) [5,10,11]. Thus, the results can be considered as representative for this joint type. The specimen's load–displacement curve until final failure is presented in Fig. 8. The displacement $L_{DIC} - L_0$ is taken from the DIC measurements (cf. Section 2.3). The load is measured by the load cell located between the servo-hydraulic cylinder and the hydraulic grips. Measurement data at the top and bottom of every cycle is influenced by friction effects of the test rig, and thus, removed from further evaluation. For the same reason, the three lowest cycles (F_{max} = 1.2 kN) show poor measurement quality, and therefore are not used any further. Cycle no. 10 (first cycle with F_{max} = 3.9 kN) shows a hysteresis which has not occurred in this magnitude up to this point. During the further test, hysteresis of the load–displacement curve is mostly present, until at cycle no. 27 (the last complete cycle), the largest hysteresis can be seen just before final rupture at cycle no. 28. Upon closer look, the load–displacement curves show a progressive behavior due to the asymmetric geometry of the SLS specimen (cf. Section 2.4).

The post-test condition of the joint surfaces is depicted in Fig. 9. Visual inspection was performed with an OLYMPUS SZX10 optical stereo microscope. Adhesive failure at the titanium-composite interface is predominant, where epoxy resin did separate cleanly from the titanium surface, with some exceptions of resin rich pockets originating from the

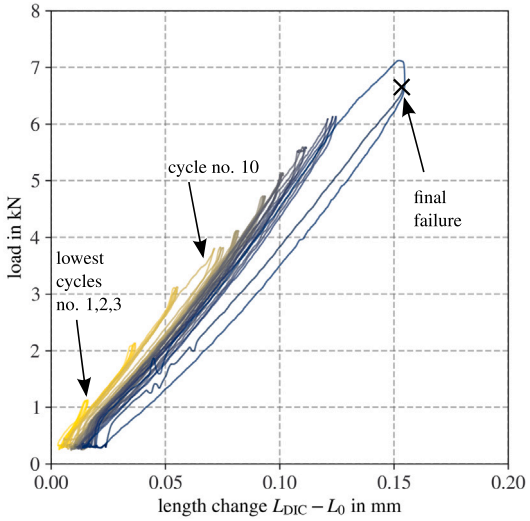

Fig. 8. Curve of length change ($L_{DIC} - L_0$) over load. For better visibility, a color gradient from yellow to blue shows the test progression from start to end.

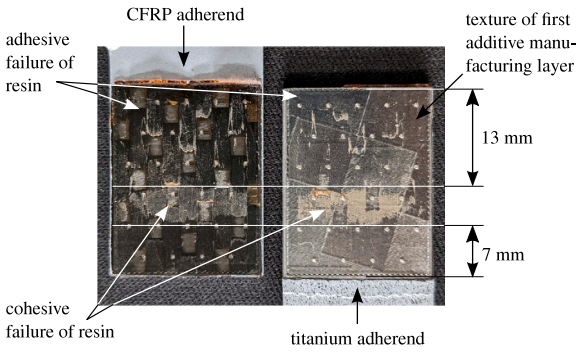

Fig. 9. Post-test ruptured joint surfaces with CFRP adherend (left) and titanium adherend (right) with determined ultimate crack lengths before failure.

fabric's weave style. On a smaller area, cohesive failure is identified by epoxy resin residue on the titanium surface. A very small amount of broken fibers is also present at this area. The transition between the two failure modes is a more or less straight line over the width of the specimen. Based on the evaluation of the DIC measurements presented later and the clearly different failure modes, this joint area is assumed to have failed during final rupture. Thus, the extent of the epoxy resin's adhesive failure zone at the titanium overlap end (13 mm) and the epoxy resin's adhesive failure zone at the CFRP overlap end (7 mm) are considered as final crack lengths just before ultimate failure. All pins failed at their roots and remain buried in the CFRP material.

3.2. Damage initiation and propagation observed by surface cracks

The damage initiation and propagation in the form of surface cracks at the overlap is observed by evaluating the correlation confidence of DIC measurements. By considering the adhesively failed overlap area at the titanium overlap end (cf. Fig. 9) as the ultimate surface crack length before final failure (cf. Section 2.3), a correlation confidence threshold of 0.0065 pixel is found. Fig. 10c presents the correlation confidence of the last recorded DIC image before specimen failure. This image is used to find the threshold. Red shading indicates threshold exceedance, and thus, cracks at the surface. The correlation confidence of the image clearly indicates a second surface crack of 7 mm at the composite overlap end, thus, validating the found threshold. Furthermore, the robustness of the crack length evaluation by the determined correlation

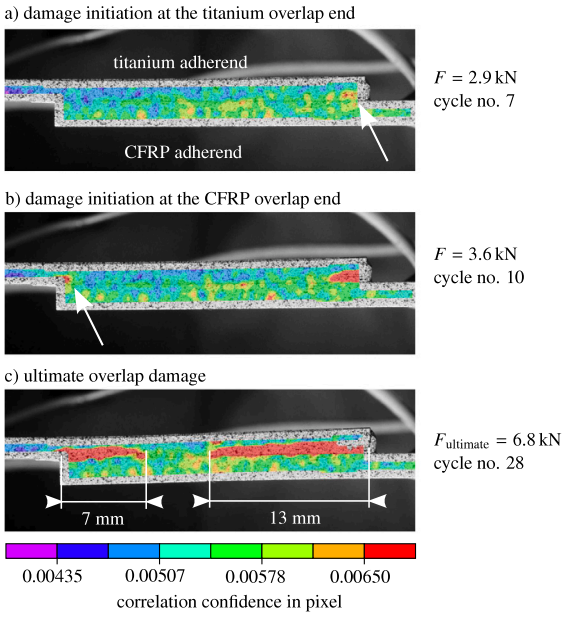

Fig. 10. DIC evaluation images, where damage initiation was identified at the (a) titanium overlap end and (b) CFRP overlap end. (c) Plot of ultimate crack lengths at the last image before specimen rupture with determined correlation confidence threshold.

confidence threshold was tested, showing only little influence for a threshold variation of ±5%. Applying the determined and validated correlation confidence threshold to DIC images throughout the experiment enables to monitor surface crack initiation and propagation. Fig. 10a presents first signs of a crack (i.e., correlation confidence threshold exceedance) at the titanium overlap end at approximately 2.9 kN during loading in cycle no. 7. Fig. 10b shows the initiation of the second crack located at the CFRP overlap end at approximately 3.6 kN during cycle no. 10. This circumstance reflects the observed hysteresis at this cycle (cf. Fig. 8). Both events of damage initiation could be determined accurately, because a sharp, local change of correlation confidence was recorded for the overlap ends from one image to the next. For a hybrid SLS joint with different stiffness properties of the adherends, the resulting shear stress along the overlap is higher at the titanium overlap end compared to the CFRP overlap end. Hence, the titanium overlap end is more prone to damage initiation, which also happened during the conducted test. As the test progresses, the formed cracks at the side surface move towards the overlap center from both ends. Overall crack propagation is faster coming from the titanium overlap end. Pin condition during the test could not be observed, since the pins were obscured by the opaque CFRP and spray paint. However, for damage propagation monitoring, the crack length is extracted for every cycle at its respective F_{max}. Correlation confidence of DIC images of selected cycles at F_{max} and the determined crack lengths are shown in Fig. 11. Paint flaking off locally resulted in small, local exceedance of the correlation confidence threshold. These locations with flaked off paint are not considered in the crack length determination. Determined crack lengths over load cycles are presented in Fig. 12. Here, the remaining intact overlap length is also plotted by subtracting the obtained crack lengths from the initial overlap length of 25.4 mm, clearly indicating the crack initiations at cycles no. 7 and 10 and the further continuous and monotonic crack propagation until final rupture.

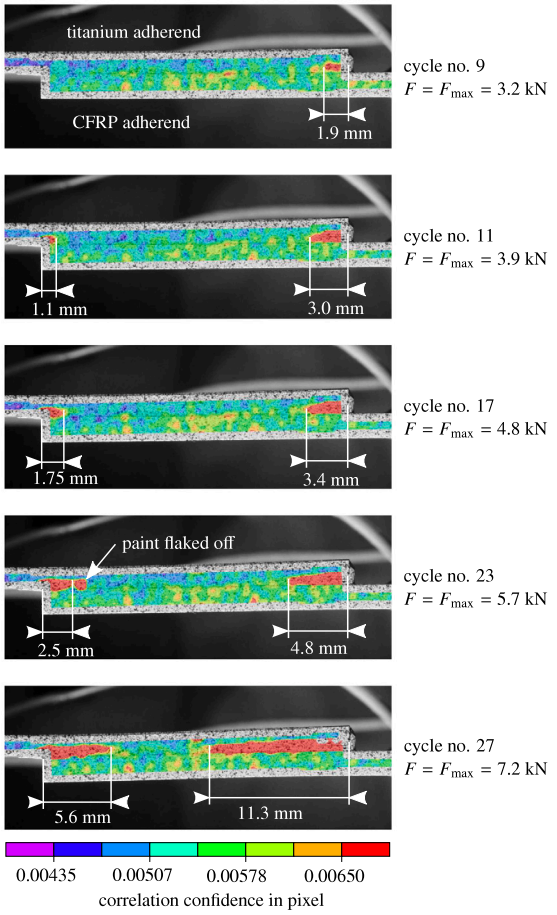

Fig. 11. Evaluation of surface crack lengths during loading, shown for five cycles, evaluated at their respective F_{max}.

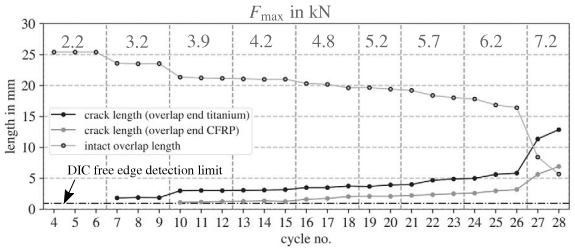

Fig. 12. Crack lengths for every cycle at F_{max} and the remaining intact overlap length.

3.3. Damage initiation and propagation observed by tangent stiffness degradation

The damage initiation and propagation at the joint is monitored by evaluating DIC measurements for tangent stiffness degradation (additionally to the previously reported surface crack observation). Therefore, the joint's tangent stiffness $k_{tan}(D)$ is calculated from the DIC measurements (cf. Section 2.4). In order to keep comparability among the load cycles throughout the test, all tangent stiffness values are evaluated during load increase within the range of 1.2 kN to 2.2 kN (this load range exists for all considered cycles). The initial tangent stiffness of the pristine joint (evaluated at cycle no. 4) is $\overline{k}^{0}_{tan}$ = 51.73 kN/mm. Mean and standard deviation of tangent stiffness over load cycles are shown in Fig. 13. At cycle no. 27 and 28, scatter in the stiffness values is very high, because during these cycles, the high degradation

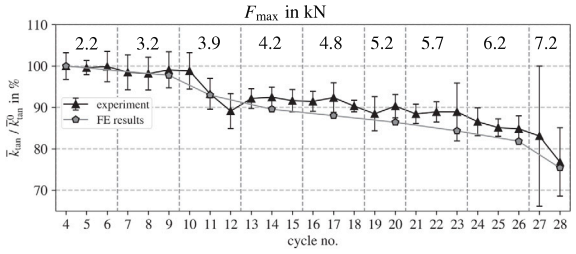

Fig. 13. Experimentally measured and numerically simulated mean tangent stiffness $\bar{k}_{tan}(D)$ during loading, normalized by pristine value, for the lowest considered load range [1.2, 2.2] in kN, (cf. Fig. 6).

of the overlap influences the obtained DIC data. The first damage initiation at cycle no. 7 reduces the mean tangent stiffness by only 1.5%, which interestingly partly recovers at cycles no. 9 and 10. With the second damage initiation at cycle no. 10, however, mean tangent stiffness decreases significantly by 10.9% until cycle no. 12. After a slight recovery at cycle no. 13 and 20, mean tangent stiffness is decreasing almost continuously to a total mean tangent stiffness loss of 23.2% just before final failure. The resulting mean tangent stiffness over the load cycles is very similar to the development of the intact overlap length (cf. Fig. 12), which demonstrates the consistency of the evaluated results. Furthermore, all structural results clearly show that although the load on the specimen is increasing throughout the experiment, the overlap fails gradually after onset of damage, which also reveals the damage tolerant failure behavior of the tested pinned hybrid composite-titanium SLS joint.

3.4. Validation of tangent stiffness change by simulation results

The validation of the tangent stiffness change is realized by FE models of the specimen and its loading condition, and calculating the joint's tangent stiffness by the simulated displacements (cf. Section 2.5). For the numerical investigation, nine different FE model configurations are created and listed in Table 4. One setup is analyzed with no overlap damage, representing the pristine state. Eight damaged states are modeled with crack lengths that represent different damage propagation stages (reported by DIC-based surface crack observation). The choice fell on cycles where the determined crack lengths fit best with the discretization of the FE model. The crack propagation front is assumed straight and the outermost pin rows behind the crack fronts are considered ruptured. This is assumed based on the post-test analysis of the DIC evaluations. Furthermore, for pinned hybrid joints in a similar test setup, compromised outer pin rows are readily reported in literature [3,5,6]. This assumption of failed pins is also supported, as FE analysis with all pin rows intact significantly overestimated the tangent stiffness compared to experimental values. This begins with cycle no. 11, where the crack at the CFRP overlap end is determined to be 3 mm long and already passed the first pin row (cf. Fig. 9). For cycle no. 11 and up to cycle no. 26, the outermost pin row at the CFRP overlap end are decoupled in the FE model. For cycle no. 28, both outermost pin rows are decoupled for FE analysis due to the significant cracks present at both overlap ends.

All FE results of tangent stiffness values (i.e., of different damage states considered) are shown in Fig. 13, averaged between a simulated loading of 1.2 kN and 2.2 kN for comparability with experimental results. Presented values are relative to the pristine FE model stiffness $\bar{k}^0_{tan,FE}$ = 62.02 kN/mm. This numerically determined value lies 19.9% higher than the experimentally found $\bar{k}^0_{tan}$. This may be explained by the model simplifications and material parameter definitions deviating from reality. However, the present FE study is used to analyze the relative tangent stiffness behavior of the joint, and thus, the model is not calibrated to the experimental results. The simulation-based values

Table 4
FE model crack length configurations for tangent stiffness analysis of different loading cycles.

Cycle no.	Crack length at overlap end in mm		Comment
	Titanium	CFRP	
Pristine	0	0	all pin rows
9	2	0	intact
11	3	1	
14	3	1.4	outermost pin
17	3.4	1.8	row at overlap
20	4	2	end titanium
23	4.8	2.5	decoupled
26	5.8	3.2	
28	11	6	outermost pin rows at both overlap ends decoupled

* According to DIC-based crack length evaluation.

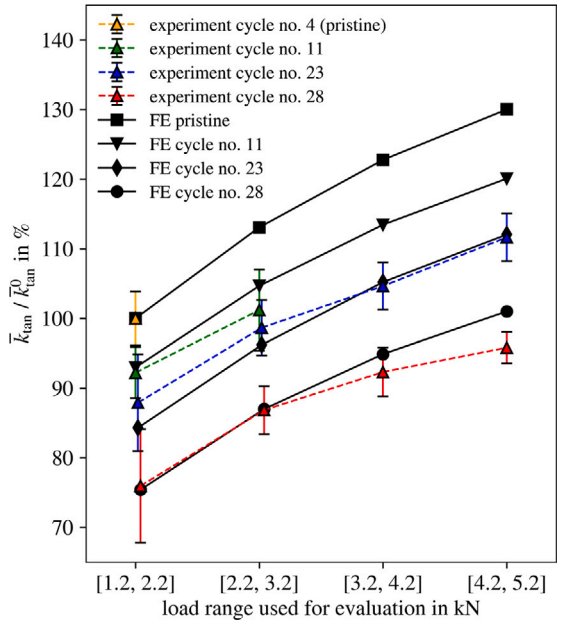

Fig. 14. FE and experimental results of mean overlap tangent stiffness for pristine and cycles no. 11, 23 and 28, according to Table 4 for higher load ranges. The mean is calculated for the four load ranges presented in Fig. 6.

show good qualitative agreement with the experimentally found tangent stiffnesses. Between cycle no. 14 and specimen failure, FE results are permanently lower than the experimental results, but they reflect the course of experimental overlap degradation well. Going further with tangent stiffness, data points are calculated not only between 1.2 kN and 2.2 kN, but also for three higher load ranges. The purpose is to show the overlap's structural behavior at increasing load. The experimentally measured as well as simulated tangent stiffness values for the four considered load ranges are presented for cycles no. 4, 11, 23 and 28 in Fig. 14. For every analyzed damage state, tangent stiffness is increasing, as load increases. With modeled damage propagation, the individual curves shift to a lower level. The experimental data shows good agreement with FE results up to specimen failure at cycle no. 28, thus, it validates the assumption on damage propagation made on the experimental observations.

3.5. Damage initiation and propagation observed by the proposed DC ERM damage indicator

The damage initiation and propagation at the considered pinned hybrid SLS joint is observed by the overlap's electrical resistance change,

as described in Section 2.2. Therefore, DC ERM of the specimen sections presented in Fig. 4 are analyzed. The measurements were done continuously for every single load cycle. Between the load cycles (i.e., at low load level F_{low}), the measurements were interrupted for other measurements, which are not part of the present research. An example of the ERM raw data is shown in Fig. 15 for cycles no. 16-18 ($F_{max} = 4.8$ kN). The raw data is linearly interpolated between the cycles to fill the gaps from the measurement pauses. Levels of measurement noise are as low as possible by the given setup, however, existing moderate noise and rare outliers are encountered. This is reduced by processing the raw data by a low pass filter before further evaluation (second order Butterworth filter, cutoff frequency $\omega_c = 3$ Hz). Rare outliers such as large spikes are removed manually. The gauge factor is determined by linear regression at the rising part of the load cycle. Calculated COD values for CFRP bulk material are above 0.9 (with exception of cycle no. 24, which is excluded due to poor measurement quality), and thus, support the linear assumption. The determined gauge factors are shown in Fig. 17a and are similar to values from literature, obtained from plain-woven CFRP bulk material [41]. For the DC ERM-relevant overlap resistance $R_{ol}(\varepsilon, D)$, the assumption of linear behavior is reasonable, but not as distinctive as for the sole CFRP bulk material. Linear regression shows COD $\geq$ 0.9 for 72% of all loading cycles and 0.7 < COD < 0.9 for 12% of all loading cycles. The remaining gauge factor values (from cycle no. 7, 8, 13 and 28) with COD < 0.7 are not presented. Stronger deviations from the linear assumption are believed to result from the damage propagation during measurement. In total, 21 out of 25 (84%) gauge factor values remain and are shown as data points in Fig. 17b. As an example, the raw and filtered data, as well as the linear regression for $R_{ol}(\varepsilon, D)$ of cycle no. 16 ($F_{max} = 4.8$ kN) is shown in Fig. 16. To obtain GF^P, all valid gauge factor values are averaged for the pristine state. According to Section 3.2, this is the case for all cycles up to cycle no. 6 ($F_{max} = 2.2$ kN), and thus, three values for the joint's pristine state are averaged for GF^P. Further, the initial resistance R_0^P (i.e., resistance at zero strain) is determined in the same way, by averaging the values from the linear regressions of the same three cycles of the pristine joint. The resulting values are $GF^P = 4.939$ and $R_0^P = 0.260\,\Omega$, which are used to calculate the pristine overlap resistance behavior $R^P(\varepsilon)$ according to Eq. (2). In Fig. 18a, the load curves of cycles no. 4 to no. 9 are shown. Fig. 18b presents the calculated electrical resistance of the pristine $R^P(\varepsilon)$ and the measured resistance $R_{ol}(\varepsilon, D)$ for these load cycles. However, the increasing discrepancy between the resistance curves (resulting from damage initiation and propagation) is highlighted in red. This discrepancy is the proposed damage indicator DI according to Eq. (4) and is presented in Fig. 18c. A corresponding trendline indicates the overall development over time. $R^d(\varepsilon, D)$ starts to deviate distinctly from zero at cycle no. 7, where first damage initiation was found by DIC-based evaluation of both surface cracks as well as tangent stiffness degradation (cf. Section 3.2). Thus, the resistance change of the overlap $R^d(\varepsilon, D)$ is clearly sensible to damage onset. However, to keep a potential influence of $O(\varepsilon, D)$ according to Eq. (3) low, the DI values are averaged for all considered load cycles at low load values (load range [1.2, 2.2] in Fig. 6a), considering the term's influence according to Fig. 18c to be negligibly small. The mean DI values per load cycle are shown together with their standard deviations in Fig. 19. The values are plotted relative to the initial resistance R_0^P, thereby, showing a clear, almost monotonic increase of the proposed DI with increasing number of load cycles. Thus, damage extent is up to 3.8% of the initial resistance until final failure. Consequently, the proposed DI is suitable for the evaluation of initiation and propagation of cracks at the overlap ends of the present pinned hybrid SLS joint.

3.6. Validation and discussion of the DC ERM method for damage monitoring

The validation of the DC ERM method with the proposed DI for the monitoring of pinned hybrid SLS joint damage initiation and propagation is already given by the previously presented results. However,

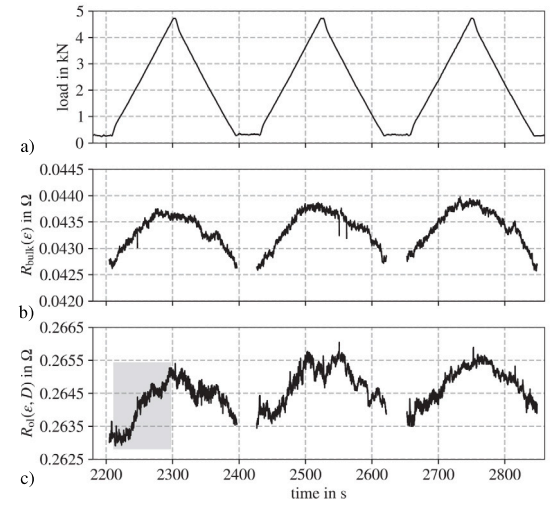

Fig. 15. Raw data for cycles no. 16, 17 and 18 with $F_{max} = 4.8$ kN. (a) load signal, (b) measured $R_{bulk}(\varepsilon)$, (c) measured $R_{ol}(\varepsilon, D)$. The gray highlighted data is used in Fig. 16 as an example for gauge factor determination.

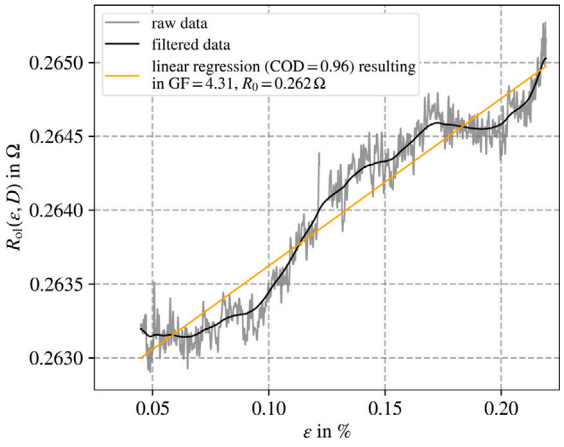

Fig. 16. Linear regression of $R_{ol}(\varepsilon, D)$ at loading cycle no. 16 ($F_{max.} = 4.8$ kN), based on the cycle's raw data shown in Fig. 15.

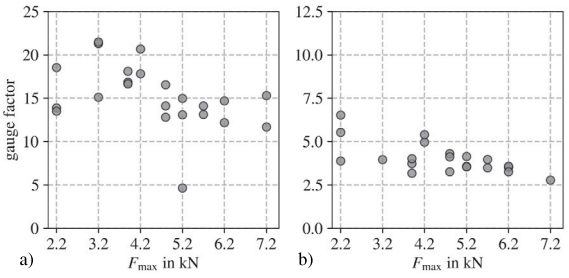

Fig. 17. Gauge factors over F_{max} for (a) CFRP bulk material, and (b) overlap bulk material mix.

for better comparability and further discussion, the various results from damage initiation and propagation monitoring during the test are summarized in Fig. 20. These are the summed up crack length and the reciprocal of the mean tangent stiffness $c = 1/k$ values (i.e., mean tangent compliance), both evaluated by DIC measurements, together with the proposed DI evaluated by DC ERM. Furthermore, the identified initiation of the two cracks at the overlap ends are indicated. The proposed DI immediately rises with the first damage initiation at the titanium overlap end, and thus, is capable of detecting

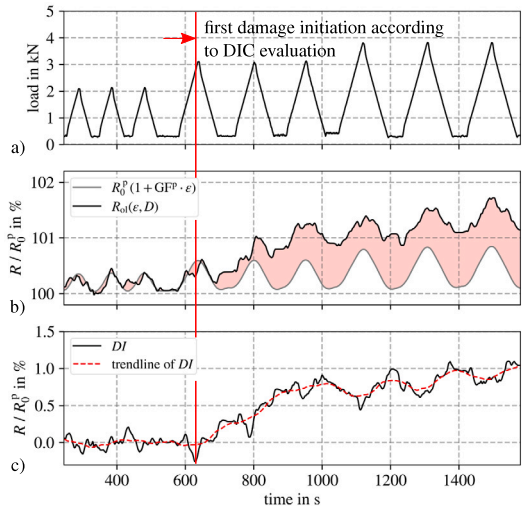

Fig. 18. (a) Load curve showing cycles no. 4-12, (b) curve of measured $R_{el}(\varepsilon, D)$ as well as calculated $R^p(\varepsilon)$, with the evolving discrepancy highlighted in red, (c) resulting damage indicator DI and its trendline.

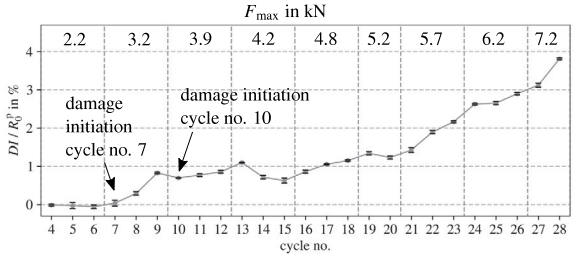

Fig. 19. Mean DI and standard deviation for every cycle during loading, for the lowest considered load range [1.2, 2.2] in kN, (cf. Fig. 6).

the considered damages at an early stage of structural degradation. In comparison, the joint's mean tangent compliance shows only little change for the first damage initiation but significantly rises with the initiation of the second crack at the CFRP adherend's overlap end. It can be assumed that the complex electrical network between the metal surface, the pins and the CFRP changed significantly, when the first damage occurred. Overall, this is traced back to the formation of new and destruction and change of old contact points within the overlap's electrical network, with the tendency towards a global, non-reversible electrical resistance increase. The initiation of the second overlap end crack in cycle no. 10 is not observable in the DI results. During the second damage initiation, the aforementioned change in the electrical contact points within he overlap's electrical network was likely not as rapid as during the first damage initiation and propagation. However, the further trend of the proposed DI over the 28 loading cycles shows a very similar behavior to both the crack lengths and the joint's mean tangent compliance. Consequently, it is also applicable for the evaluation of the damage propagation and seems promising for damage size evaluation (SHM level 3), or with other words, it may be used to evaluate the remaining, intact overlap length. However, this is not part of the present research. An exact localization of the first damage initiation seems challenging with a single DC ERM value. This may be solved by an additional electrical contact at the joint's overlap, but it is not considered meaningful, as it is of little importance for the joint's structural integrity. This is particularly true when thinking about real overlaps in structural components, where the location along the joint and its lateral extent are more relevant for its integrity. A practical implementation of DC ERM for SHM could be the array-like monitoring of pinned hybrid SLS joint lines. The systematic measurement of the

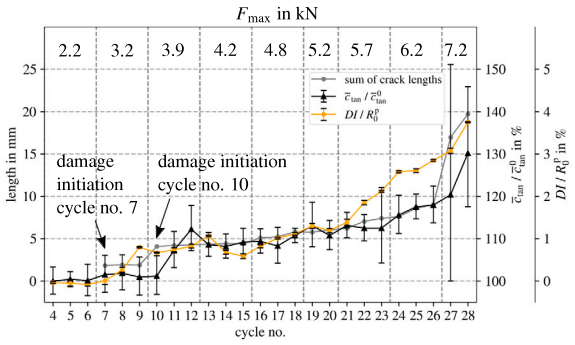

Fig. 20. Comparison of the summed up crack length, mean tangent compliance and mean DI values for the load range [1.2, 2.2] in kN, averaged for every cycle during loading, (cf. Fig. 6).

electrical resistance of the joint's overlap and evaluation techniques for spatial reconstruction of electrical properties such as the electrical impedance tomography are believed to enable both localization and size estimation of damages at pinned hybrid SLS joints (SHM level 2 and 3). Thus, considering the damage type (cracks at the overlap ends) as a-priori knowledge, DC ERM of pinned hybrid joints with a SLS geometry may enable full damage identification for SHM application (SHM level 4). However, this needs to be investigated and demonstrated at larger structural elements and is left for future research.

4. Conclusions and outlook

The present research investigates and demonstrates the DC ERM method for damage initiation and propagation monitoring on pinned hybrid SLS joints with adherends made of titanium and CFRP, respectively. For method application, no costly electrical modifications like e.g., adding conductivity-enhancing substances to the joint are needed. For DC ERM-based damage evaluation, a load-independent DI is proposed, which represents the non-reversible resistance change of the joint's overlap, due to the joint's propagating failure in the form of cracks at the overlap ends. Results clearly show the high sensitivity of the used DI for first crack initiation at the titanium overlap end. Furthermore, the DI is also capable of monitoring the overlap's crack propagation until final failure, and thus, also has a high potential for damage quantification. The demonstration of the proposed DI comes along with a comprehensive structural analysis of the used case example of a pinned hybrid SLS joint specimen by both experimental DIC measurements and FE-based simulations. As implied by literature for similar pinned hybrid joints, crack formation at the overlap ends is identified as the predominant initial failure mode to be monitored, which could be reproduced in the present study. This initial damage propagates from both overlap ends along the overlap until final failure of the joint. The pin array interferes with this damage propagation, resulting in damage tolerance of the joint, and thus, demonstrates its suitability for aviation components in combination with SHM. All results discussed here are limited to the considered configuration of a pinned composite-titanium SLS specimen under uniaxial, quasistatic loading. However, the mechanical degradation behavior of the pinned hybrid SLS specimen well reflects results described in literature, and thus, is considered representative as proof-of-concept of the ERM-based damage evaluation. Nevertheless, the degradation typically scatters for such complex joints. Consequently, the reported sensitivity of the presented DC-ERM based SHM method is expected to vary between and within joint designs (e.g., smaller relative change of electrical potential values due to larger overlaps or lower number of pins, etc.). Future investigations are needed that address these issues by e.g., studies on larger sample sizes to reveal the method's damage size-dependent Probability of Detection (POD). In particular, these studies shall address

the statistical significance of damage size and location evaluation and expand the method to its application for larger structural elements by means of electrical contact arrays.

CRediT authorship contribution statement

Andreas Dengg: Conceptualization, Data curation, Formal analysis, Investigation, Methodology, Validation, Writing – original draft. **Christoph Kralovec:** Conceptualization, Methodology, Project administration, Writing – review & editing. **Martin Schagerl:** Conceptualization, Funding acquisition, Project administration, Writing – review & editing.

Declaration of competing interest

The authors declare that they have no known competing financial interests or personal relationships that could have appeared to influence the work reported in this paper.

Data availability

Data will be made available on request.

Acknowledgments

This research was conducted within the SUSTAINair project. This project has received funding from the European Union's Horizon 2020 research and innovation program under grant agreement No. 101006 952. The authors would like to thank the DLR Institute of Materials Research (Köln, Germany) and INVENT GmbH (Braunschweig, Germany) for specimen production.

References

[1] Wahab MA. Chapter 5 - composite to metal. In: Joining composites with adhesives: Theory and applications. Destech Publications, Inc.; 2016.
[2] Ucsnik S, Scheerer M, Zaremba S, Pahr DH. Experimental investigation of a novel hybrid metal-composite joining technology. Composites A 2010;41:369–74. http://dx.doi.org/10.1016/j.compositesa.2009.11.003.
[3] Parkes PN, Butler R, Meyer J, de Oliveira A. Static strength of metal-composite joints with penetrative reinforcement. Compos Struct 2014;118:250–6. http://dx.doi.org/10.1016/j.compstruct.2014.07.019.
[4] Parkes PN, Butler R, Almond DP. Fatigue of metal-composite joints with penetrative reinforcement. In: Proceedings of the 54th AIAA/ASME/ASCE/AHS/ASC structures, structural dynamics, and materials conference. Boston, Massachusetts, USA; 2013, p. 1879. http://dx.doi.org/10.2514/6.2013-1879.
[5] Graham DP, Rezai A, Baker D, Smith PA, Watts JF. The development and scalability of a high strength, damage tolerant, hybrid joining scheme for composite-metal structures. Composites Part A: Appl Sci Manuf 2014;64:11–24. http://dx.doi.org/10.1016/j.compositesa.2014.04.018.
[6] Huelsbusch D, Haack M, Solbach A, Emmelmann C, Walther F. ti-cfrp hybrid structures produced by laser additive manufacturing. 2015.
[7] Sarantinos N, Kostopoulos V, Vita GD, Campoli G, Bricout L. Micro-pins: the next step in composite–composite and metal–composite joining. CEAS Space J 2019;11:351–8. http://dx.doi.org/10.1007/s12567-019-00251-1.
[8] Habenicht G. Kleben. Berlin Heidelberg: Springer-Verlag; 2006.
[9] Goland M, Reissner E. The stresses in cemented joints. J Appl Mech 1944;11:A17–27. http://dx.doi.org/10.1115/1.4009336.
[10] Parkes P, Butler R, Almond D. Growth of damage in additively manufactured metal-composite joints. In: Proceedings of the ECCM15—15th European conference on composite materials. Venice, Italy; 2012, p. 24–8.
[11] Ramaswamy K, O'Higgins RM, Corbett MC, McCarthy MA, McCarthy CT. Quasi-static and dynamic performance of novel interlocked hybrid metal-composite joints. Compos Struct 2020;253. http://dx.doi.org/10.1016/j.compstruct.2020.112769.
[12] Rytter A. Vibrational based inspection of civil engineering structures (Ph.D. thesis), Denmark; 1993.
[13] Kralovec C, Schagerl M. Review of structural health monitoring methods regarding a multi-sensor approach for damage assessment of metal and composite structures. Sensors 2020;20. http://dx.doi.org/10.3390/s20030826.
[14] Abry J, Bochard S, Chateauminois A, Saliva M, Giraud G. In situ detection of damage in CFRP laminates by electrical resistance measurements. Compos Sci Technol 1999;59:925–35. http://dx.doi.org/10.1016/S0266-3538(98)00132-8.
[15] Abry J, Choi Y, Chateauminois A, Dalloz B, Giraud G, Salvia M. In-situ monitoring of damage in CFRP laminates by means of ac and dc measurements. Compos Sci Technol 2001;61:855–64. http://dx.doi.org/10.1016/S0266-3538(00)00181-0.
[16] Zhao Q, Zhang K, Zhu S, Xu H, Cao D, Zhao L, et al. Review on the electrical resistance/conductivity of carbon fiber reinforced polymer. Appl Sci 2019;9:2390. http://dx.doi.org/10.3390/app9112390.
[17] Angelidis N, Wei C, Irving P. The electrical resistance response of continuous carbon fibre composite laminates to mechanical strain. Composites A 2004;35. http://dx.doi.org/10.1016/j.compositesa.2004.03.020.
[18] Chung DDL. Structural health monitoring by electrical resistance measurement. Smart Mater Struct 2001;10:624. http://dx.doi.org/10.1088/0964-1726/10/4/305.
[19] Till A, Karsten J, Kötter B, Fiedler B. Health monitoring of scarfed CFRP joints under cyclic loading via electrical resistance measurements using carbon nanotube modified adhesive films. Composites A 2018;105:150–5. http://dx.doi.org/10.1016/j.compositesa.2017.11.015.
[20] Lim AS, Melrose ZR, Thostenson ET, Chou T-W. Damage sensing of adhesively-bonded hybrid composite/steel joints using carbon nanotubes. Compos Sci Technol 2011;71. http://dx.doi.org/10.1016/j.compscitech.2010.10.009.
[21] Nauman S. Piezoresistive sensing approaches for structural health monitoring of polymer composites — A review. Eng 2021;2:197–226. http://dx.doi.org/10.3390/eng2020013.
[22] Baek S-J, Kim M-S, An W-J, Choi J-H. Defect detection of composite adhesive joints using electrical resistance method. Compos Struct 2019;220(7). http://dx.doi.org/10.1016/j.compstruct.2019.03.081.
[23] ASTM D5868-01: Standard test method for lap shear adhesion for fiber reinforced plastic (FRP) bonding. 2014.
[24] Dutta B, Froes FH. The additive manufacturing of titanium alloys. Butterworth-Heinemann; 2016, http://dx.doi.org/10.1016/B978-0-12-804782-8.00001-X.
[25] HexForce® HS06K carbon fabric G0926 D 1304 TCT INJ E01-2F product data sheet. Hexcel Corporation; 2021.
[26] HexPly® 913 product data sheet. Hexcel Corporation; 2020.
[27] Peng H. Using laser etching to improve surface contact resistance of conductive fiber filler polymer composites. International Publication Number WO 02/19346 A1, World Intellectual Property Organization; 2001.
[28] Swaminathan S, Ozutemiz KB, Majidi C, Hudson SE. Fiberwire: Embedding electronic function into 3D printed mechanically strong lightweight carbon fiber composite objects. In: Proceedings of the 2019 CHI conference on human factors in computing systems. Glasgow, Scotland, UK; 2019, p. 1–11. http://dx.doi.org/10.1145/3290605.3300797.
[29] Todoroki A, Suzuki K, Mizutani Y, Matsuzaki R. Durability estimates of copper plated electrodes for self-sensing CFRP composites. J Solid Mech Mater Eng 2010;4:610–20. http://dx.doi.org/10.1299/jmmp.4.610.
[30] Bisagni C, Furfari D, Pacchione M. Experimental investigation of reinforced bonded joints for composite laminates. J Compos Mater 2017;52:431–47. http://dx.doi.org/10.1177/0021998317708021.
[31] Output variables in Vic-2D and Vic-3D, Application Note, Correlated Solutions Inc.
[32] Vic-2D Reference manual, Correlated Solutions Inc.
[33] Sutton M, Orteu J-J, Schreier H. Image correlation for shape, motion and deformation measurements. Basic concepts, theory and applications. Springer Science & Business Media; 2009.
[34] Heinzlmeier L, Sieberer S, Schagerl M. Fatigue and progressive damage of thin woven CFRP plates weakened by circular holes. Exp. Mech. 2023;1–13. http://dx.doi.org/10.1007/s11340-023-00956-9.
[35] Murray B, Fonteyn S, Carrella-Payan D, Kalteremidou K-A, Cernescu A, Van Hemelrijk D, et al. Crack tip monitoring of mode I and mode II delamination in CF/Epoxies under static and dynamic loading conditions using digital image correlation. In: Proceedings of the 18th international conference on experimental mechanics. Brussels, Belgium; 2018, http://dx.doi.org/10.3390/ICEM18-05225.
[36] Rogani A, Navarro P, Marguet S. Study of post-impact behaviour of thin carbon/epoxy laminates subject to fatigue tensile loading. Int J Fatigue 2021;148:106134. http://dx.doi.org/10.1016/j.ijfatigue.2020.106134.
[37] Thäsler T, Holtmannspötter J, Gudladt H-J. Monitoring the fatigue crack growth behavior of composite joints using in situ 2D-digital image correlation. J Adhes 2019;95:595–613. http://dx.doi.org/10.1080/00218464.2018.1562923.
[38] Dassault systemes abaqus/cae. https://www.3ds.com/products-services\/simulia/products/abaqus/abaquscae/.
[39] TIMETAL® 6-4, 6-4 ELI & 6-4-.1Ru, Medium to high strength general purpose alloys. Titanium metals corporation; 2000.
[40] Schürmann H. Konstruieren mit Faser-Kunststoff-Verbunden. Berlin Heidelberg: Springer-Verlag; 2005.
[41] Nurprasetio IP, Budiman BA, Afwan AA, Halimah PN, Utami ST, Aziz M. Nonlinear piezoresistive behavior of plain-woven carbon fiber reinforced polymer composite subjected to tensible loading. Appl Sci 2020;10. http://dx.doi.org/10.3390/app10041366.

Update

Composite Structures

Volume 340, Issue , 15 July 2024, Page

DOI: https://doi.org/10.1016/j.compstruct.2024.118168

Composite Structures 340 (2024) 118168

Contents lists available at ScienceDirect

Composite Structures

journal homepage: www.elsevier.com/locate/compstruct

Corrigendum

Corrigendum to "Damage monitoring of pinned hybrid composite-titanium joints using direct current electrical resistance measurement" [Compos. Struct. 334 (2024) 117972]

Andreas Dengg [a,*], Christoph Kralovec [a], Miriam Löbbecke [b], Jan Haubrich [b], Martin Schagerl [a]

[a] Institute of Structural Lightweight Design, Johannes Kepler University, Altenberger Straße 69, Linz, 4040, Upper Austria, Austria
[b] Institute of Materials Research, German Aerospace Center, Linder Höhe, Cologne, 51147, Germany

The authors regret that the names of some contributors were inadvertently omitted from the original version of the article. The names of the omitted authors are Miriam Loebbecke and Jan Haubrich, both from the Institute of Materials Research, German Aerospace Center (DLR; Deutsches Zentrum fuer Luft- und Raumfahrt e.V.), Linder Höhe, 51147 Cologne, Germany. They developed the geometry and pattern of the reinforcing pins shown in Figure 1. In addition, they developed the additive manufacturing parameters for the titanium component and provided them for the investigations presented in the article. Therefore, Miriam Löbbecke and Jan Haubrich are added as authors for their contribution by providing resources. The authors apologize for any inconvenience caused.

CRediT authorship contribution statement

Andreas Dengg: Conceptualization, Data curation, Formal analysis, Investigation, Methodology, Validation, Writing – original draft. **Christoph Kralovec:** Conceptualization, Methodology, Project administration, Writing – review & editing. **Miriam Löbbecke:** Resources. **Jan Haubrich:** Resources. **Martin Schagerl:** Conceptualization, Funding acquisition, Project administration, Writing – review & editing.

Declaration of competing interest

The authors declare that they have no known competing financial interests or personal relationships that could have appeared to influence the work reported in this paper.

Data availability

No data was used for the research described in the article.

DOI of original article: https://doi.org/10.1016/j.compstruct.2024.117972.
* Corresponding author.
E-mail address: andreas.dengg@jku.at (A. Dengg).

https://doi.org/10.1016/j.compstruct.2024.118168
Received 23 April 2024; Accepted 28 April 2024
Available online 17 May 2024